An Automated Live Imaging Platform for Studying Merozoite Egress-Invasion in Malaria Cultures

Alex J. Crick,[†] Teresa Tiffert,[‡] Sheel M. Shah,[†] Jurij Kotar,[†] Virgilio L. Lew,[‡] and Pietro Cicuta[†*]
[†]Cavendish Laboratory and [‡]Department of Physiology, Development and Neuroscience, University of Cambridge, Cambridge, UK

ABSTRACT Most cases of severe and fatal malaria are caused by the intraerythrocytic asexual reproduction cycle of *Plasmodium falciparum.* One of the most intriguing and least understood stages in this cycle is the brief preinvasion period during which dynamic merozoite–red-cell interactions align the merozoite apex in preparation for penetration. Studies of the molecular mechanisms involved in this process face formidable technical challenges, requiring multiple observations of merozoite egress-invasion sequences in live cultures under controlled experimental conditions, using high-resolution microscopy and a variety of fluorescent imaging tools. Here we describe a first successful step in the development of a fully automated, robotic imaging platform to enable such studies. Schizont-enriched live cultures of *P. falciparum* were set up on an inverted stage microscope with software-controlled motorized functions. By applying a variety of imaging filters and selection criteria, we identified infected red cells that were likely to rupture imminently, and recorded their coordinates. We developed a video-image analysis to detect and automatically record merozoite egress events in 100% of the 40 egress-invasion sequences recorded in this study. We observed a substantial polymorphism of the dynamic condition of pre-egress infected cells, probably reflecting asynchronies in the diversity of confluent processes leading to merozoite release.

INTRODUCTION

A major limitation in our understanding of the molecular mechanisms behind the brief and random cell-cell interactions that mediate fundamental biological processes in many organisms is the difficulty of optically imaging such events under the microscope, on live specimens, with the control, frequency, and detail required for a proper investigation. To elucidate the molecular mechanisms involved, one would optimally seek to record such interactions with high-speed videomicroscopy, minimal phototoxic effects, and good resolution in *x-y-z* space on a sufficient number of events for statistical analysis, under controlled experimental conditions, and with the appropriate optical indicators. For random and infrequent interactions, a major additional hurdle is the correct location of the right fields at the right times, to enable the required number of observations to be made during the period of sample viability.

One particular and important instance of such brief cell-cell interactions that can be studied in culture conditions under the microscope is the process of merozoite egress from human red blood cells (RBCs) infected with the malaria parasite *Plasmodium falciparum* (*Pf*), followed by invasion of new RBCs by freshly released merozoites (1,2,3–7,8–10,11). Here we used this process to guide the development and test the performance of an automated platform for observing and recording multiple egress-invasion events under controlled experimental conditions. During these tests, we observed a marked polymorphism of pre-egress dynamics. The results establish the viability of automatic detection and recording of multiple egress-invasion events, an essential feasibility test for the new robotic imaging platform.

First, we briefly review the background relevant to the biological system used in this study, and some of the open issues involving merozoite egress. The merozoite egress process has been the subject of intense interest in the last decade (1,12,4,5,9). The asexual reproduction cycle of *Pf* parasites in human RBCs lasts ~48 h. In the few minutes preceding merozoite release, infected RBCs (iRBCs) appear to swell under osmotic stress and acquire a flower-like appearance, with a crown of merozoite petals surrounding a central pigment, the remnant of the hemozoin-filled digestive vacuole (1,6,7). Using a mathematical-computational model of the homeostasis of malaria-infected RBCs (13,14), Lew (8) showed that there was enough colloidosmotic pressure left on the residual hemoglobin concentration of the host red cell to provide the driving force for the observed swelling if pre-egress membrane cation permeability experienced a terminal increase. Using fluorescent membrane markers, Glushakova et al. (4) showed that upon rupture, the membrane of the host red cell is converted to a bunch of linked vesicles. Using state-of-the-art high-speed videomicroscopy and epifluorescence, Abkarian et al. (1) recently revealed the dynamic morphology of the host cell membrane from rupture to the vesiculated end-state: At the initial opening, a single merozoite emerges and is assumed to be propelled by the hydrostatic pressure gradient that occurs after terminal swelling. Immediately after this, the membrane around the opening first curls outward to form a circular toroid around the opening, and then rapidly curls further

Submitted September 10, 2012, and accepted for publication January 15, 2013.

*Correspondence: pc245@cam.ac.uk

Editor: Michael Edidin.

0006-3495/13/03/0997/9 $2.00

http://dx.doi.org/10.1016/j.bpj.2013.01.018

backward, buckles, turns inside out (eversion), and vesiculates, all in ~400 ms, favoring the rapid and unhindered ejection and dispersal of the remaining merozoites. The egress sequence of curling, buckling, eversion, and vesiculation (CBEV) of the host cell membrane was found to be analogous to the sequence that can be generated experimentally in membranes from uninfected RBCs in the process of spontaneous vesiculation, albeit over a much slower time course. This analogy was interpreted as the exploiting of an intrinsic biological potential by the parasite, requiring specific remodeling of the RBC cortical cytoskeleton for a rapid CBEV response during normal egress (9).

From this brief description, it becomes clear that a number of complex processes must concur to ensure successful egress with rapid dispersal of the released merozoites, which is critical for optimizing the invasion of new RBCs and for reproductive cycle continuity. These prerupture processes include terminal merozoite maturation, parasitophorous vacuolar membrane breakdown, osmotic swelling, protease activation, and cytoskeletal priming for a rapid CBEV sequence. The confluence of such different processes may be expected to generate variations in the appearance of prerupture iRBCs. Although we could not anticipate the modality and nature of the variations, alert observation of the dynamic morphology of prerupture iRBCs in a large sample of records allowed us to provide what is to our knowledge the first description of the polymorphism associated with this stage.

The work reported here can be thought of as the design stage of an automated robotic platform, aiming at the specific requirement of recording large numbers of egress-invasion events on live samples with optimal space and time resolution. It was important to systematically record paired egress-invasion events, because only successful invasion events after egress confirm the infective viability of the released merozoites, a key test of adequate culture conditions and egress normality (5,7,15). It is hoped that the automatic imaging platform will prove a key tool for future research on random cell-cell interactions in general, and in particular for investigating the mechanisms by which the initial contact between merozoite and red cell compels red cell motility to aid in the apical alignment of the merozoite, an essential yet poorly understood preliminary step to invasion (3,10).

We investigated the characteristics of the pre-egress and egress stages in search of the optimization criteria to be incorporated into the controlling software for the recognition and tagging of pre-egress candidate iRBCs. This investigation required the biological material to be set up for long periods of observation under the microscope in normal culture conditions and with minimal phototoxic exposure. More than 40 egress-invasion sequences were recorded, allowing a number of phenotypic observations to be made.

MATERIALS AND METHODS

Here we describe the preparation of the biological material and the experimental setup for the detection and analysis of large numbers of egress-invasion events in the context of building the automated imaging platform.

Preparation of *Pf* schizont-enriched samples for long-term microscopic observation

Direct observation of egress-invasion events requires a mix of uninfected RBCs and iRBCs containing late-stage parasites (schizonts) from a synchronized culture to be placed in a special chamber under the microscope, where the culture conditions can be continued for extended periods of time to enable the collection of sufficient data on paired egress-invasion events under comparable conditions. A primary concern is to ensure the right proportion of uninfected to infected cells to provide sufficient invasion targets next to freshly released merozoites whose infectivity is short-lived, but without crowding the field of view with overlapping cells (5). We followed slightly modified variations of the methods originally reported by Dvorak et al. (3) and Glushakova et al. (4–7). Red cells infected with *Pf* A4 clone derived from the ITO4 line were cultured under a low-oxygen atmosphere by standard methods as previously described (16,17). The culture medium was changed daily and consisted of RPMI-1640 supplemented with 40 mM HEPES (N-2-hydroxyethylpiperazine-N-2-ethanesulfonic acid), 25 mg/L gentamicin sulfate, 10 mM D-glucose, 2 mM glutamine, and 0.5% vol/vol albumax (Sigma-Aldrich, UK). Synchronization was performed by alternating sorbitol lysis (18) and gelatin flotation (19,20). A final gelatin flotation procedure was carried out immediately before each experiment to separate and use the top, schizont-enriched fraction of iRBCs. Parasitemia was set to 10% by the addition of uninfected RBCs to provide the required proportion of uninfected RBCs to iRBCs, and the hematocrit was set to 0.2% in culture medium to provide optimal cell packing without overlapping and to ensure sufficient space for released merozoites attempting invasion to be monitored.

Cell imaging

Cells were imaged in Secure-Seal hybridization chambers with 200 μL overall capacity (Sigma-Aldrich), mounted on glass slides. A custom-built temperature-control stage was used to maintain the optimal culture temperature of 37°C during imaging experiments. The microscope slide was placed in contact with a copper block, with electrical resistors attached to either side of the block. A thermocouple was attached to the glass slide to measure local temperature, and a PID controller adjusted the current sent through the resistors in a feedback loop with the thermocouple.

Imaging, both automated and manual, was done on a Nikon TI-Eclipse inverted microscope with a 60× water objective (NA 1.2); all the motorized functions of the microscope stand were controlled via software written in-house running on a PC under a Linux operating system. Images were acquired with an AVT Pike F100B camera connected via FireWire to the control PC; videos were recorded at up to 100 frames per second, and images were simultaneously passed on (on a separate computational thread) via shared memory to be analyzed in real time by the automation software described below. The video-analysis feeds back to the instrument control, enabling the platform to automatically perform imaging tasks such as searching for egress candidates and other actions described in the Outlook section.

Image filters selection for egress detection

Pre-egress monitoring

Software development for the automated detection of iRBC candidates with impending egress required translation of descriptive morphology to

quantitative sensors of the pre-egress–egress sequence. This was implemented with the use of image analysis filters.

A variety of filters for pre-egress schizont detection were tested on a preliminary subset of pre-egress records before they were integrated into the live microscopy system. iRBCs were easily identified among the cells in any field of view by their hemozoin crystals, which were compacted within the residual body. They were located via intensity thresholding and pixel clustering, filtered through specific boundaries of size and shape (Fig. 1, *A* and *B*).

To image the cell membrane, we found 360 membrane edge points by analyzing the intensity bleeps on the radial profiles emanating from each hemozoin crystal (Fig. 1 *C*). The edge points were used to characterize the cell under observation and to determine its viability as a candidate for imminent egress (as characterized in preliminary observations), based on its mean radius, circularity (radius variance), and mean edge strength (magnitude of the maximum intensity gradient averaged over 360 radial profiles). Repeated detection of the membrane edge points also allowed us to track cell shape and orientation changes over a series of consecutive images.

Egress detection

Consistent and immediate detection of egress events required computationally light image analysis filters to provide parameters that when tracked over time would produce reliably sharp signals immediately upon egress. A host of potential filters was considered, and each was tested and optimized across the preliminary data pool. The filters labeled DarkThresh and BrightThresh monitored the contributions, summed over a boxed region surrounding the cell, of the low tail and high tail of the intensity histogram, respectively. The PixelSubtraction filter reported the summation of the individual pixel differences between consecutive frames (i.e., the differences, summed over a boxed region around the cell, between the pixel intensity in one frame and the corresponding pixel intensity in the next frame). The MeanRadius and Circularity filters quantified geometric parameters derived from the cell contour points, and the AvemaxGrad filter measured the mean edge strength around the contour.

Image analysis was typically performed at ~0.1 s per frame (1000 × 1000 pixels) per field of view, with motorized movement to an adjacent field of view taking ~0.2 s. In addition to tracking iRBCs to correct for lateral motion, the focus score of the cell chosen as a focus target was updated for every frame. The focus score was generated from the area under the tails (top and bottom 5%) of the intensity histogram for the iRBC, a quantity that was found to show a strong z dependence, having an approximate minimum in a plane of good focus. When this value exceeded a set threshold, implying that defocusing had occurred, the motorized z position of the microscope objective was adjusted until the focus score of the target cell returned to within its allowed boundary.

The membrane edge points detected and updated for each candidate iRBC in each frame were used to build comparison arrays for the three optical parameter filters (MeanRad, Circularity, and PixelSubtraction) that were employed to detect parasitic egress events promptly. The means and standard deviations (SDs) of the parameter filters were first calculated at the commencement of cell tracking and subsequently updated for every frame in which none of the filters produced a signal. Comparison of detection filters between separate frames depended on a chosen lag time, which also defined the size of the comparison arrays. Because images may be analyzed faster (up to 0.1 s) than the time taken for a typical egress event (~0.4–0.6 s (1)), a sharper signal is produced when the detection filters in nonconsecutive frames are compared. A lag time of ~10 frames (1 s) was found to be optimal, although this decreased as more fields of view were included in the tracking process.

RESULTS AND DISCUSSION

The critical initial step in the development of an automated system to monitor egress-invasion events in live *Pf* cultures is to optimize the detection of iRBC schizont-stage candidates that are likely to rupture and release merozoites within minutes of entering the observation field. To that end, we analyzed the behavior of pre-egress iRBCs to identify the characteristics that might be used in optical filters to optimize automated detection. Our starting selection of iRBC candidates was guided by the early observations of Glushakova and collaborators (6,7), who established that in the pre-egress period, iRBCs acquire a round configuration in which the compacted, hemozoin-dense residual body is clearly visible and often morphs into a terminal flower-like shape in which bulging merozoites appear surrounding a residual body located near the center. Our preliminary work, over extended periods of direct observations, confirmed this description and set the basic criteria for pre-egress candidacy selection. We consider first the dynamic state of the pre-egress candidates analyzed here.

Variability in appearance and dynamic behavior of pre-egress iRBCs

We recorded 50 iRBC pre-egress candidates that showed a flower-like appearance and an adequate surrounding of uninfected RBCs without cell overlaps (Fig. 2). Of these, 40 were eventually paired to successful subsequent invasion events, resulting in an egress-invasion pairing rate of ~80% in our sample. Successful invasion was judged by the appearance of at least two recognized morphological indicators of invasion (3), namely, apical alignment and penetration, ring formation, and postinvasion echinocytosis (Fig. 3). It should be noted that the observed egress-invasion pairing rate represents a lower-bound estimate of invasive viability because post-egress invasion also depends on

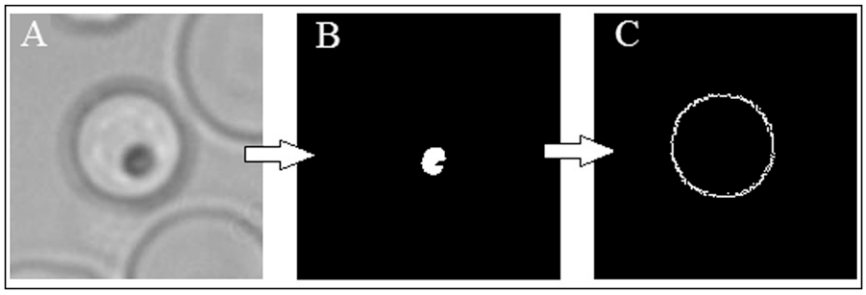

FIGURE 1 Key image analysis steps in the identification, localization, and shape characterization of pre-egress schizont candidate cells. (*A*) Bright-field image (60× water objective) of a near-spherical schizont candidate. (*B*) Hemozoin crystal detection by intensity thresholding and pixel clustering. (*C*) Cell membrane contour obtained by analysis of the intensity bleeps detected along 360 radial profiles emanating from each hemozoin crystal.

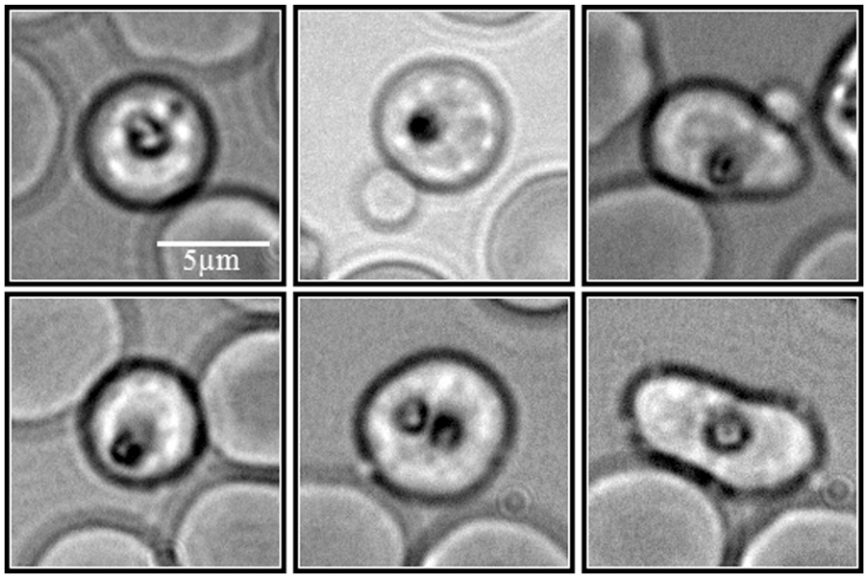

FIGURE 2 Varied morphology of six pre-egress schizont candidates. The iRBCs in these six examples were imaged in bright field with a 60× objective, within the last 10 min period pre-egress. Transient departures from apparent sphericity were observed as part of the dynamic shape changes that occurred during the pre-egress period. All of these cells were followed through a successful egress-invasion sequence.

random local factors such as the availability of uninfected red cells that could be targeted for invasion along the dispersal directions of the released merozoites.

Within the egress-invasion sample, we noted a remarkable variety of dynamic behaviors of the iRBCs prior to egress. At one end, we observed largely quiescent iRBCs that hardly changed in appearance over periods of up to 60 min, from first detection until rupture (see Movie S1 in the Supporting Material). At the other end of the spectrum, very dynamic iRBCs were seen intermittently or continuously changing shape and orientation, as inferred by the eccentric displacements of the residual body, with rapid light-shade surface changes reflecting internal large-scale motions, membrane bulging and retracting, and reversible exovesiculation events (see Fig. 2, Movie S2, Movie S3, and Movie S4). The quiescent (Q) or dynamic (D) pre-egress condition did not show any detectable correlation with the pattern of merozoite release and dispersal after rupture (see Table 1).

Possible effects of illumination

An important caveat to bear in mind when interpreting our results, which is applicable to all optical studies on live cell samples in culture, concerns the possible effects of illumination. In vivo, egress-invasion events occur in the microvasculature in the absence of photo-exposure in the visible wavelength range. In vitro, the illumination required for observation makes it necessary to take into account potential phototoxic effects. Wissing et al. (21) showed that exposure of *Pf*-infected RBCs with mature-stage parasites to high-frequency light (<500 nm wavelength) for periods of up to 20 min caused strong cytoplasmic acidification when the global photon exposure exceeded 0.2 mol/m^2. They demonstrated that acidification resulted from disruption of the parasite's acidic food vacuole brought about by lipid peroxidation, which was initiated in turn by light-induced generation of hydroxyl radicals. The shutter wavelength used for their observations between exposures was 680 nm, a lower-energy wavelength that is assumed to minimize phototoxic effects. In our study, we employed optical filters to block transmission of wavelengths below 650 nm, and thus significantly reduced the damaging effects from higher-energy components of the spectrum. Furthermore, illumination levels were kept at the minimum required for image resolution. Using an Andor iXon3 single photon detection EMCCD camera, we measured the photon

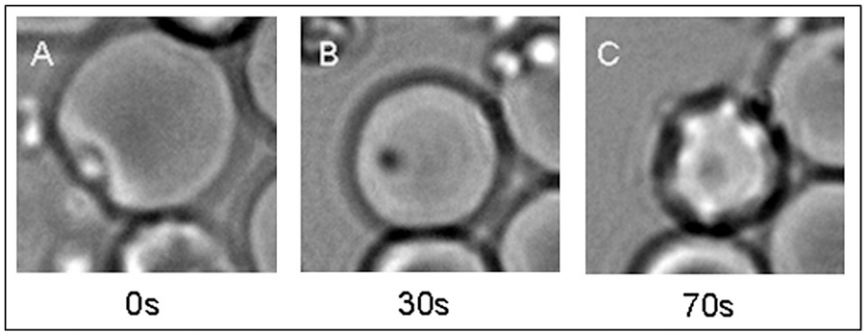

FIGURE 3 Selected frames illustrating sequential events during invasion in live imaging assays. (*A*) Apical alignment and penetration. (*B*) Early ring formation. (*C*) Postinvasion echinocytic deformation, lasting for up to 10–20 min (3). *A-C* was the most frequently recorded invasion indicator pair.

TABLE 1 Comparison of morphological and dynamic parameters of Q- and D-type pre-egress and egress modalities

	Q	D
$<R_s>$ (μm) (population mean ± SD)	4.0 ± 0.2	3.8 ± 0.3
$<R_{s\text{-}5min}>$ (μm) (population mean ± SD)	4.0 ± 0.2	4.1 ± 0.5
($<R_{s\text{-}5min}>$ - $<R_{egress}>$) (μm) (population mean)	0.00	0.35
$<RMS_s>$ (population mean, negl. SD)	1%	2%
$<RMS_{s\text{-}5min}>$ (population mean ± SD)	(1 ± 0)%	(15 ± 10)%
$<RMS_{s\text{-}5min}>$ - $<RMS_{egress}>$ (population mean)	0%	13%
Egress duration (s) (population mean ± SD)	0.8 ± 0.2	0.8 ± 0.2
V_{max} of leading merozoite (μm/s) (population mean ± SD)	71 ± 14	70 ± 12
R_m/R_s, 3 s post-egress (mean ± SD)	1.5 ± 0.2	1.6 ± 0.2

$<R_s>$ and $<R_{s\text{-}5min}>$ are the schizont mean radii measured immediately before and 5 min before egress, respectively. $<RMS_s>$ is the root mean-square deviation of the schizont radius from its mean, giving a measure of anisotropy. $<RMS_{s\text{-}5min}>$ is the same measurement made 5 min before egress (egress duration is measured from the first appearance of an extracellular merozoite to the point at which all visible merozoites are judged to be free of the host cell membrane). V_{max} is the maximum escape velocity measured for the leading merozoite in an egress event (as described in Figs. 7 and 8). R_m is the estimated dispersion radius of the merozoite group measured 3 s after the onset of egress. V_{max} was measured for 10 viable events, R_m was measured for 34 events, and all other quantities were measured for 50 events.

flux for the imaging conditions applied in our study at ~4 × 10^{16} photons/(m^2s), equivalent to 0.07 μmol/(m^2s). Due to the longer wavelength of the illumination light, photon power density was also significantly lower (0.013 W/m^2, roughly equivalent to 1 Lux of luminous flux). In principle, it is impossible to completely rule out illumination effects on the pre-egress polymorphism. Heterogeneities in host cell age, metabolic status, or cytoskeletal state, for instance, may condition selective schizont vulnerabilities to low-energy photon exposure. However, we found no correlation between the duration of the optical exposure period and any of the pre-egress features that characterized the dynamic behavior. For example, we observed reversible exovesiculation in samples that were exposed to light for nearly 1 h pre-egress as well as in samples that were exposed for only 5 min before egress. Nevertheless, it is clear that many more observations will be needed to completely exclude contributions of light-exposure to pre-egress dynamics.

Filter imaging of the pre-egress–egress transition

Fig. 4 *A* illustrates the application of the six selected filters (see Materials and Methods) to track a typical pre-egress-egress sequence over 10 s, to cover the last few seconds before the egress event. The signal strength from each filter is reported relative to the mean noise level for that signal as a function of frame number for image records taken at 10 frames per second. It can be seen that whereas all six filters produced a temporal signal for the egress event, only three filters—MeanRadius, Circularity, and PixelSubtraction—

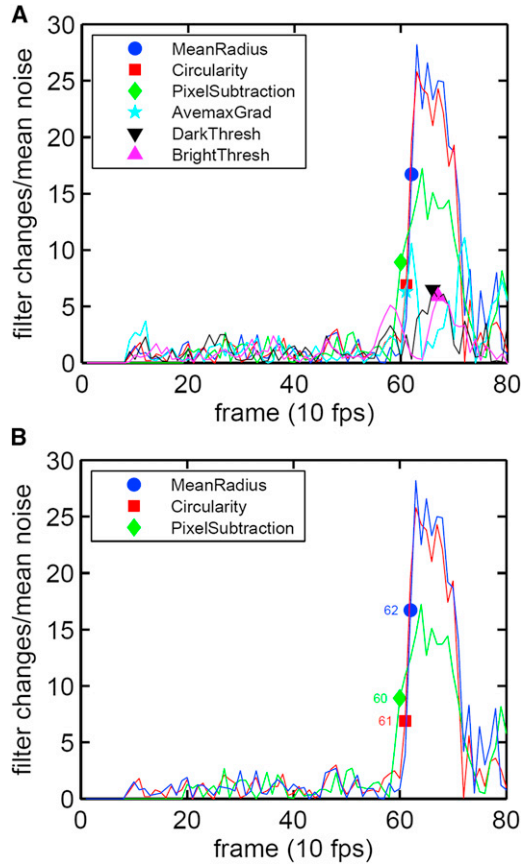

FIGURE 4 Filter responses to a typical pre-egress–egress sequence tracked over a period of 10 s, before and after the egress event. (*A*) Response of all six tested image filters to an example egress event. The signal strength from each filter is reported relative to the mean noise level for that signal. Image records were taken at 10 frames per second. (*B*) Selected responses of the three filters with the strongest and most consistent signals. The numbers next to the markers on the steep upward deflection of each trace report the frame number in which each filter first registered a significant egress-related signal; these numbers are shown to illustrate the tight synchronicity of filter detection.

produced a signal with a substantially high signal/noise ratio. The separate response of the three selected filters is shown in Fig. 4 *B* and it reflects the consistent pattern observed over the preliminary data pool.

When the filters were tested individually, each one was able to detect most (but not all) of the egress events in the sample. The most common reason for individual filter failures over some events was a false positive triggered by a vigorous pre-egress dynamic change (described below and in Fig. 6), or an effective increase in the background noise level of the filter signals, again due to pre-egress dynamics. The success or failure of a filter or a combination of filters to properly detect an egress event proved to be highly dependent upon selecting the appropriate threshold for the filter signal. The threshold was defined as the number of SDs above the mean noise level of the pre-egress regime that would constitute an event. The threshold in this case is a measure of the signal strength required before an event is

deemed to have occurred. If it is set too low, this threshold produces an overly sensitive detector that seemingly detects false-positive egresses but is unable to distinguish between a real event and the additional noise contributions brought about by pre-egress morphological dynamics. At the other end, if the threshold is set too high, the detector becomes insensitive and ignores genuine egress events. No individual filter or pair of filters was found to have perfect efficiency.

In search of the optimum detection of egress by the filter signals, we tested different algorithmic combinations of the three chosen filter signals on the full sample of iRBCs. Fig. 4 illustrates the algorithmic combination that provided an egress-detection success rate of 100%, resulting in the most robust detection system. We found the optimum combination by requiring that any two of the three filters must report a signal above 5 σ, and the third must report a signal above 0.5 σ. We called this the A+B+0.5*C combination. A, B, and C in Fig. 5 are interchangeable with any of the three filters, i.e., A can be MeanRad (M), Circularity (C), or PixelSubtraction (P), and B and C can be one of the remaining filters. Thus, there are six possible permutations (M-C-P, M-P-C, C-M-P, C-P-M, P-M-C, and P-C-M) that are evaluated at each time point. As can be seen in Fig. 5, a global signal threshold of $\sigma = 5$ proved optimal for successfully and consistently detecting egresses.

Comparison of quiescent and dynamic pre-egress forms: morphology, dynamics, and invasive efficiency

In our sample of 40 egress-invasion events, 24 showed the quiescent pattern and 16 displayed different variations of dynamic behavior.

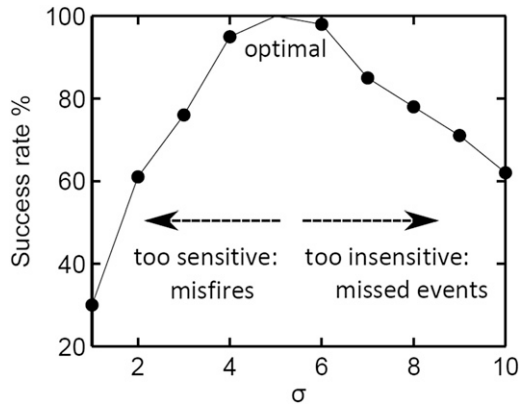

FIGURE 5 Success rate for detection of egress events as a function of the signal combination threshold. The detection success rate for egress events across the data pool is plotted as a function of the number of SDs above the pre-egress noise level (σ) at which the signal threshold was set for each filter. The three image filter signals for MeanRadius, Circularity, and PixelSubtraction are used in the algorithmic combination A+B+0.5*C, where A, B, and C denote any of the filters, and the combination requires that two of the three filters reach the σ threshold and one reaches 0.5 σ. Optimal detection success was obtained with $\sigma = 5$.

Fig. 6 shows an example of how the normalized signals from the MeanRadius (Fig. 6 *A*) and Circularity (Fig. 6 *B*) filters report pre-egress dynamics in the few seconds preceding egress. The egress event is exposed by the sharp drop of the filter signals reflecting the collapse of the membrane edge. Before egress occurs, the traces from a quiescent iRBC (*dark gray*) show a steady pattern with minor drifts and fluctuations. On the other hand, the traces from an iRBC with a dynamic changing morphology show variable fluctuations preceding the egress (*light gray*). Although the figure shows only the last few seconds pre-egress, the patterns illustrate behavior that was monitored for up to 60 min for the different iRBCs.

In Fig. 7 we explore whether pre-egress dynamics, as registered by the fluctuation pattern described in Fig. 6 *A*, has any effect on the delay time to invasion. The results suggest a trend in which iRBCs with quiescent pre-egress patterns (*dark columns*) deliver merozoites, and most of these merozoites tend to invade new RBCs earlier than those

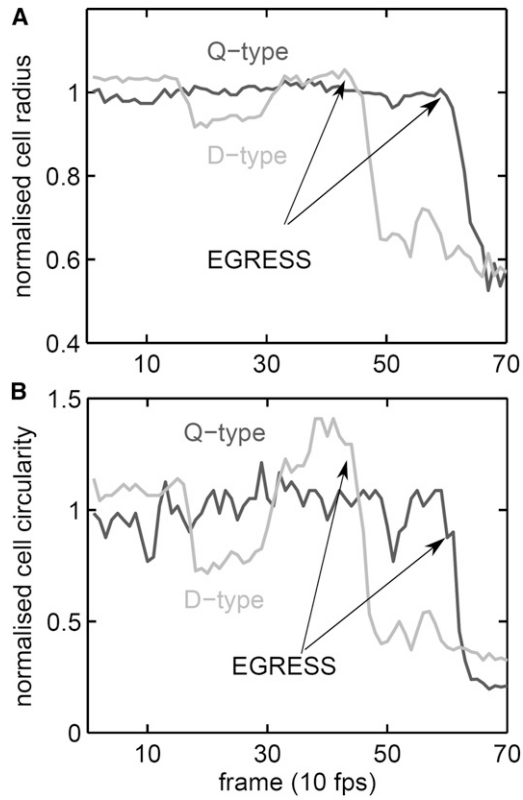

FIGURE 6 (*A* and *B*) Pre-egress dynamic condition of iRBCs as represented by the outputs of the MeanRadius (*A*) and Circularity (*B*) filters. The filter traces were normalized by their means over the pre-egress period and are shown as a function of time before, during, and after egress. Q-type (*black trace*): quiescent condition; D-type (*gray trace*): dynamic condition. The sample shown is representative of the two conditions in the full dataset. The egress event is indicated by a sharp drop in all mean-normalized traces reflecting edge collapse. The residual signal/noise ratio post-egress results from edge points assigned to the cell center, thus reducing the mean radius and the variance in the mean radius (circularity).

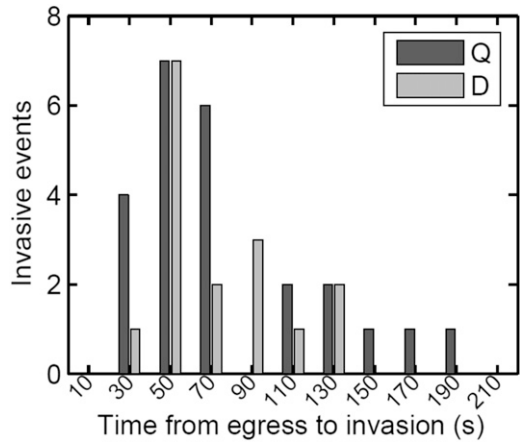

FIGURE 7 Delay time to merozoite invasion after egress from iRBCs with quiescent (Q, *dark columns*) or dynamic (D, *gray columns*) pre-egress patterns. Results from all 40 egress-invasion events recorded are shown.

originating from cells with dynamic egress patterns (gray columns). Q-type released merozoites also appear to sustain a longer invasive potential, with invasions occurring up to 3 min after egress. The comparison assumes that other factors that affect invasion efficiency, such as the mean distances between released merozoites and invasion target red cells, would have affected the quiescent and dynamic groups similarly, as defined by the filter test applied. A much larger sample will be needed to establish whether these trends are significant, and to allow a comparison of the invasion efficiencies of merozoites released from Q and D iRBCs. The observed Q-D polymorphism may simply reflect the manner in which the different processes that have to concur at egress (briefly described in the Introduction) happen to influence the pre-egress dynamic morphology of the iRBCs.

In Fig. 8 we explore the dynamics of egress over a typical Q-type egress event, following the approach originally used by Abkarian et al. (1). The mean dispersion radius, R_m, of the daughter merozoites is measured 3 s after the onset of egress, and can be compared with R_s, the mean radius of the schizont from which the daughters emerged. The leading merozoite is also tracked over time from its first extracellular appearance to provide a measure of its velocity during the egress process. Fig. 9 shows the leading merozoite velocity for the egress event shown in Fig. 8. It can be seen that there is an extremely fast initial escape, followed by rest periods and further peaks corresponding to the escape of subsequent individual merozoites pushing the initial parasite from behind. This profile is in broad agreement with that originally reported by Abkarian et al. (1). In addition, in Movie S5, as in most of our egress records, the curling-eversion components of the CBEV sequence discovered by those authors can be clearly seen.

The peak escape velocity of the leading merozoite, V_{max}, and the dispersion ratio, R_m/R_s, were measured across a range of Q- and D-type egress events. These values, along with other morphological and dynamic properties used in the comparison of Q- and D-type forms, are summarized in Table 1. Over the population sample, D-type schizonts

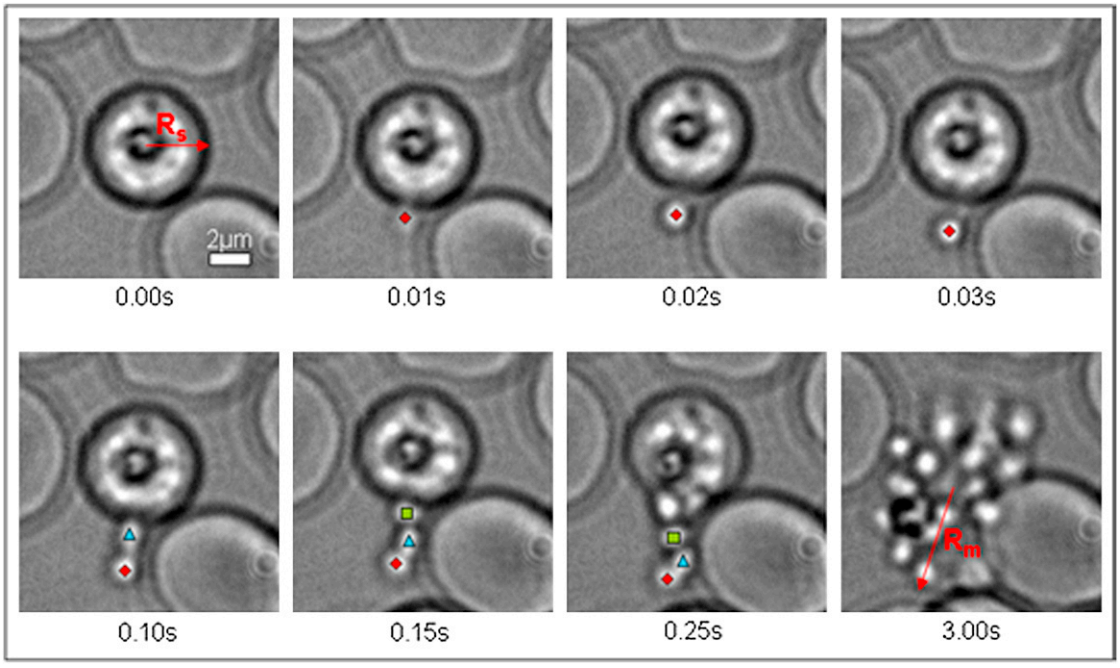

FIGURE 8 Merozoite egress sequence recorded at 97 frames per second with a 60× objective (NA 1.2). Selected frames of a typical egress sequence (Q-type) are shown. The three leading merozoites after initial escape are easily identified and tracked manually (positions shown with markers), and the coordinates of the leading one (◆) are used to calculate the dispersion distance and velocity, as reported in Table 1. R_s is the mean radius of the schizont immediately before egress; R_m is the approximate radius of the dispersed merozoite group 3 s after the onset of egress.

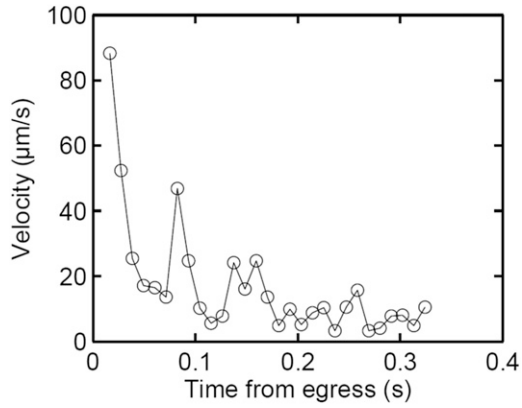

FIGURE 9 Velocity profile of the leading merozoite in the egress sequence of Fig. 8 shows the burst modality of merozoite egress. The points report the velocity obtained from displacements of the merozoite between consecutive frames, beginning from its first extracellular appearance. The results show an extremely fast initial escape followed by rest periods, and further peaks corresponding to the escape of subsequent individual merozoites pushing the initial merozoite from behind. This oscillating trend is common to all of the egress events and is in broad agreement with earlier observations (1).

are shown to decrease both their mean radius and anisotropy over the 5 min before egress, in contrast to Q-type forms, which remain remarkably constant. Interestingly, there are no significant differences between Q- and D-type forms across the remaining morphological and dynamic parameters measured here.

Outlook

We recorded and analyzed 50 pre-egress–egress sequences in live *Pf* cultures, followed by invasion events in 40 instances (see Movie S6). The results 1), establish the feasibility of automatic detection of multiple egress-invasion events; 9), provide that the algorithmic procedure to be applied to selected image filter traces to minimize false positives or missed events, and; 3), document variations in the dynamic morphology of the pre-egress stage. This recording platform is operational and has the ability to detect egresses at a rate that is at least an order of magnitude greater than manual experiments can achieve, without operator fatigue and with a greatly reduced demand for man-hours.

We outline here how this advance will be developed into a flexible automated recording platform. Automated observation and recording of egress-invasion events can be achieved through a coupling of software-controlled microscopy and real-time in situ image analysis. The analysis program produces data that feed back to hardware controls for comparisons between sequential image frames, in a continual loop of tracking and comparison. The image analysis algorithm can be readily extended to encompass cells in several different fields of view to be tracked simultaneously by moving the motorized stage. A move of the stage to an adjacent field of view takes ~0.2 s. The resulting decrease in temporal sensitivity may limit egress detection, but for the purposes of studying invasion dynamics, this method would be able to track on the order of 15–20 schizonts simultaneously, thus providing an optimal alternative for building statistically robust datasets of brief cell-cell interaction events.

After detection of an egress event, not only is the video recording kept in expanding libraries available for future quests, but a range of other actions can also be initiated promptly. For example, the field of view may be narrowed to include only the area surrounding the released parasites, to increase the frame rate for invasion observations. Rapid-focus oscillations may be instigated, with chosen amplitude and frequency, to monitor invasion dynamics simultaneously on several planes, while allowing for sporadic refocusing of the image to counter hysteresis in the z motors. Imaging conditions can be changed from bright-field/phase contrast to fluorescence, e.g., to monitor calcium signals. Automated optical trapping maneuvers may also be designed and implemented to test parasite motility and adhesion in the time period immediately after egress (22). These are just a few of the possible actions that the automation system may take when an egress is detected.

A major application envisaged for the robotic imaging platform is the investigation and elucidation of the molecular mechanism underlying the preinvasion events that lead to apical alignment of the merozoites before penetration occurs (10). The preinvasion stage was shown to be of key importance for controlling invasion efficiency (23), but remains one of the least-understood stages of the parasite's intraerythrocytic cycle. We hope that the imaging platform under development will provide the critical tool for such investigations and prove to be of use in the study of many other cell-cell interactions of biological and medical relevance.

CONCLUSIONS

In this work, we have described automated imaging of *Pf* egress events. In the video datasets used to develop and calibrate the system, we observed remarkably heterogeneous egress phenotypes and measured their properties. These variations are most likely due to variability in the timing of several processes that lead to merozoite release.

Our long-term objective is to develop this work further, to enable a software-controlled robotic system. This system will automatically recognize multiple schizont-stage iRBCs that are considered good pre-egress candidates and track them simultaneously under wide-field observation or by scanning over multiple fields of view. Detection of egress events will prompt immediate activation of an x-y-z focusing and rapid z-scanning routine with a high NA objective, to record the preinvasion and penetration stages of

merozoite-RBC interactions with optimal resolution and depth reconstruction. Upon recognition of invasion cessation, the system will rapidly return to monitoring further egress events, thus allowing efficient statistics-building datasets.

SUPPORTING MATERIAL

Captions for supplemental movies are available at http://www.biophysj.org/biophysj/supplemental/S0006-3495(13)00088-X.

This work was supported by a Doctoral Training Accounts award from the Engineering and Physical Sciences Research Council to A.J.C., a Churchill Scholarship to S.M.S., and a Human Frontier Science Program grant (RGY0069/2009) to J.K.

REFERENCES

1. Abkarian, M., G. Massiera, …, C. Braun-Breton. 2011. A novel mechanism for egress of malarial parasites from red blood cells. *Blood.* 117:4118–4124.
2. Dvorak, J. A., L. H. Miller, …, T. Shiroishi. 1975. Invasion of erythrocytes by malaria merozoites. *Science.* 187:748–750.
3. Gilson, P. R., and B. S. Crabb. 2009. Morphology and kinetics of the three distinct phases of red blood cell invasion by Plasmodium falciparum merozoites. *Int. J. Parasitol.* 39:91–96.
4. Glushakova, S., G. Humphrey, …, J. Zimmerberg. 2010. New stages in the program of malaria parasite egress imaged in normal and sickle erythrocytes. *Curr. Biol.* 20:1117–1121.
5. Glushakova, S., J. Mazar, …, J. Zimmerberg. 2009. Irreversible effect of cysteine protease inhibitors on the release of malaria parasites from infected erythrocytes. *Cell. Microbiol.* 11:95–105.
6. Glushakova, S., D. Yin, …, J. Zimmerberg. 2007. Quantification of malaria parasite release from infected erythrocytes: inhibition by protein-free media. *Malar. J.* 6:61–65.
7. Glushakova, S., D. Yin, …, J. Zimmerberg. 2005. Membrane transformation during malaria parasite release from human red blood cells. *Curr. Biol.* 15:1645–1650.
8. Lew, V. L. 2005. Malaria: endless fascination with merozoite release. *Curr. Biol.* 15:R760–R761.
9. Lew, V. L. 2011. Malaria: surprising mechanism of merozoite egress revealed. *Curr. Biol.* 21:R314–R316.
10. Lew, V. L., and T. Tiffert. 2007. Is invasion efficiency in malaria controlled by pre-invasion events? *Trends Parasitol.* 23:481–484.
11. Salmon, B. L., A. Oksman, and D. E. Goldberg. 2001. Malaria parasite exit from the host erythrocyte: a two-step process requiring extraerythrocytic proteolysis. *Proc. Natl. Acad. Sci. USA.* 98:271–276.
12. Balu, B., S. P. Maher, …, J. H. Adams. 2011. CCR4-associated factor 1 coordinates the expression of Plasmodium falciparum egress and invasion proteins. *Eukaryot. Cell.* 10:1257–1263.
13. Lew, V. L., T. Tiffert, and H. Ginsburg. 2003. Excess hemoglobin digestion and the osmotic stability of *Plasmodium falciparum*-infected red blood cells. *Blood.* 101:4189–4194.
14. Mauritz, J. M., A. Esposito, …, V. L. Lew. 2009. The homeostasis of Plasmodium falciparum-infected red blood cells. *PLOS Comput. Biol.* 5:e1000339.
15. Trager, W. 2002. On the release of malaria merozoites. *Trends Parasitol.* 18:60–61.
16. Esposito, A., J. B. Choimet, …, T. Tiffert. 2010. Quantitative imaging of human red blood cells infected with Plasmodium falciparum. *Biophys. J.* 99:953–960.
17. Tiffert, T., H. Ginsburg, …, V. L. Lew. 2000. Potent antimalarial activity of clotrimazole in in vitro cultures of Plasmodium falciparum. *Proc. Natl. Acad. Sci. USA.* 97:331–336.
18. Lambros, C., and J. P. Vanderberg. 1979. Synchronization of *Plasmodium falciparum* erythrocytic stages in culture. *J. Parasitol.* 65:418–420.
19. Jensen, J. B. 1978. Concentration from continuous culture of erythrocytes infected with trophozoites and schizonts of Plasmodium falciparum. *Am. J. Trop. Med. Hyg.* 27:1274–1276.
20. Pasvol, G., R. J. M. Wilson, …, J. Brown. 1978. Separation of viable schizont-infected red cells of *Plasmodium falciparum* from human blood. *Ann. Trop. Med. Parasitol.* 72:87–88.
21. Wissing, F., C. P. Sanchez, …, M. Lanzer. 2002. Illumination of the malaria parasite Plasmodium falciparum alters intracellular pH. Implications for live cell imaging. *J. Biol. Chem.* 277:37747–37755.
22. Mauritz, J. M., A. Esposito, …, C. F. Kaminski. 2010. Biophotonic techniques for the study of malaria-infected red blood cells. *Med. Biol. Eng. Comput.* 48:1055–1063.
23. Tiffert, T., V. L. Lew, …, N. Mohandas. 2005. The hydration state of human red blood cells and their susceptibility to invasion by Plasmodium falciparum. *Blood.* 105:4853–4860.